Title

CryoEM of ATP-driven dynamics and itraconazole binding in a fungal ABC pump

Jorgaq Pata[1,2], Benjamin Wiseman[3]†, Eleftherios Zarkadas[4]†, Rim Baccouch[1], Nour Samrouth[1], Célia Desbois[1], Loïck Moissonier[1], Alexis Moreno[1,5], Atanu Banerjee[6], Stéphanie Aguerro[7], Emmanuel Bettler[7], Marie Dujardin[5,8], Raphaël Terreux[7], Guy Schoehn[4], Martin Högbom[3], Ahcène Boumendjel[9], Erwin Lamping[10], Richard D Cannon[10], Rajendra Prasad[6], Vincent Chaptal[1]* and Pierre Falson[1]*

[1] Drug Resistance & Membrane Proteins group, Molecular Microbiology & Structural Biochemistry Laboratory, CNRS - Lyon 1 University 5086, IBCP, Lyon, France

[2] Current address: Center for Soft Nanoscience, Busso Peus 10, 48149, Münster, Germany.

[3] Department of Biochemistry and Biophysics, Arrhenius Laboratories for Natural Sciences, Stockholm University, Stockholm, Sweden.

[4] University of Grenoble Alpes, CNRS, CEA, EMBL, IBSG, F-38000 Grenoble, France.

[5] Eurofins-CALIXAR, 60 avenue Rockefeller, Lyon, France

[6] Amity Institute of Biotechnology and Amity Institute of Integrative Sciences and Health, Amity University Haryana, Gurgaon, India

[7] ECMO team, Tissue Biology and Therapeutic Engineering Laboratory, CNRS - Lyon 1 University Laboratory 5305, IBCP, Lyon, France

[8] Current address: mRNA Center of Excellence, Analytical Sciences, Sanofi, 1541 Avenue Marcel Mérieux, 69280 Marcy l'Etoile, France

[9] University of Grenoble Alpes, INSERM, LRB, Grenoble, France

[10] Department of Oral Sciences, Sir John Walsh Research Institute, University of Otago, Dunedin, New Zealand

* Correspondence to Pierre Falson (pierre.falson@univ-lyon1.fr; pfalson@me.com) and Vincent Chaptal (vincent.chaptal@cnrs.fr)

† These authors contributed equally to this work

Azole resistance in *Candida* species often results from overexpression of the ABC transporter Cdr1, which expels drugs via ATP-driven conformational changes. Despite its clinical relevance, the structural basis of Cdr1 function has remained elusive. Here, we present four high-resolution cryo-EM structures of *Candida glabrata* Cdr1 under active turnover with ATP-Mg^{2+}, itraconazole, and vanadate. Itraconazole is seen to curve deeply into the drug-binding pocket. A deep exploration of the variability within these particle datasets uncovered 80 transient conformations, including two nucleotide-bound states—one closed and one open—that capture, for the first time, the conformational transitions triggered by ATP hydrolysis in both nucleotide-binding and transmembrane domains. At the catalytic site, motion initiates in the C-helix adjacent to the ABC signature motif, retracting 4 Å from the γ-phosphate/vanadate position. This movement, transmitted to nearby TMH-1, opens the drug-binding site via its lateral displacement. A second set of conformations reveals coordinated rearrangements of transmembrane helices that drive substrate extrusion. These findings provide a direct structural and dynamic framework for understanding Cdr1-mediated azole resistance, and, more broadly, illuminate the conserved chemo-mechanical cycle of nucleotide-binding domains across the ABC superfamily, including non-membranous members.

Fungi infect more than 300 million people world-wide with an estimated 6.5 million of them developing severe invasive infections and ~2.5 million casualties each year[1]. Fungi also infect plants and animals, causing the loss of one-third of global agricultural production[2]. Human infections are mainly caused by *Candida* species, opportunistic fungi that can invade tissues of immunocompromised hosts, such as those undergoing surgery or co-infected with other microorganisms[3]. Most of these infections are caused by the commensal yeast *Candida albicans*; however, other *Candida* species, such as *C. glabrata*[4] and *C. auris*[5], are of an increasing concern due to their reduced or complete lack of sensitivity to antifungal therapies.

Fungicidal and fungistatic drugs have been developed to combat these infections[6] by targeting yeast-specific biosynthetic pathways[7]. Azoles are the most widely used antifungals, accounting for approximately 25% of the market[8]. These drugs bind to Cyp51[6,9], inhibiting the demethylation of ergosterol precursors —the lipid that constitutes 20% of yeast membranes[10].

As a first line of defense against azole antifungals, fungi overexpress membrane proteins that act as pumps to expel azole antifungals from the cytoplasm, preventing their action[11,12]. In *Candida* species, the most prominent protein belongs to the ATP-binding cassette (ABC) superfamily[13-15], namely *Candida* drug resistance 1 (Cdr1). The protein shares 55 to 70% sequence identity with the pleiotropic drug resistance 5 (Pdr5) transporter of *Saccharomyces cerevisiae* (Supplementary Figure 1).

This resistance phenotype has typically been reported in patients for whom fluconazole-based therapy failed to eradicate *C. glabrata* infections[16]. This phenotype is illustrated in panels a and b of Figure 1, where the clinical *C. glabrata* strain DSY562, initially sensitive to fluconazole (EC_{50} ~33 μM), reacts by triggering the overexpression of Cdr1 through a mutation in its transcription factor Pdr1[16], as schematized in panel c. The resulting strain DSY565 is fully insensitive to fluconazole and remains sensitive to itraconazole but at a concentration 10 times higher than that required to inhibit the growth of DSY562 (EC_{50} ~223 nM *vs*. 27 nM). The upregulation of these ABC efflux pumps also confers resistance to many other drugs due to their ability to bind and

expel structurally diverse compounds, a phenotype initially identified as pleiotropic drug resistance (PDR)[17]. About one-third of all yeast ABC transporters are PDR transporters[13,14].

PDR transporters are ~ 1,500-residue long polypeptides organized as pseudo-dimers, with two transmembrane domains (TMDs), each composed of six TM helices (TMHs), and two cytoplasmic nucleotide-binding domains (NBDs). The NBDs alternately dimerize and dissociate to form two nucleotide-binding sites (NBSs) (Figure 1c). Compounds to be exported bind to a drug-binding site (DBS) located at the interface of the two TMDs and are expelled in the cell exterior by a mechanism powered by ATP binding and hydrolysis at the NBSs.

In PDR exporters, these domains form two NBD-TMD tandems in a characteristic type V subfamily topology[18]; for a review see[19-21]. The first NBS –NBS-1– consists of the Walker A and B motifs of NBD-1 and the ABC signature motif, also referred to as the C-loop of NBD-2. It binds but does not hydrolyze ATP due to substitutions of key catalytic residues and is referred to hereafter as ^{nc}NBS for "non-catalytic nucleotide-binding site". The second NBS –NBS-2– consists reciprocally of the Walker A and B motifs of NBD-2 and the ABC signature motif of NBD-1. It binds and hydrolyzes ATP and is referred to hereafter as the catalytic NBS, ^{c}NBS (Figure 1c).

Structural information, both static and dynamic, is still lacking in explaining the evolutionary adaptation that rendered NBS-1 non-catalytic. However, our teams and others have highlighted its critical importance both in Pdr5[22,23] and in *Ca*Cdr1[24,25]. In each case, the drug-susceptibility phenotype of primary single mutants located at the periphery of the outer leaflet region of the TMD was reported to be reverted by secondary single mutants located in the ^{nc}NBS, far from the primary mutation. Notably, one of these secondary mutants involves the glutamine residue of the ABC Signature motif – Q1002 in *Ca*Cdr1 (1005 in *Cg*Cdr1) – suggesting a close functional relationship between these regions, the structural basis of which remains unknown. See for a review[20].

Recently, the cryo-EM structures of functional Pdr5 reconstituted in peptidiscs provided the first molecular-level insights into the organization of PDR exporters[26]. In contrast, obtaining structural information on *Candida* PDR transporters has been more challenging, primarily due to difficulties in preserving the functional integrity of these proteins outside their native membrane environment. Thus, structural information from a fully functional *Candida* PDR exporter is still lacking, preventing a complete understanding of how these pumps confer protection against azole antifungals.

Here, we first describe several high-resolution cryo-EM structures of *C. glabrata Cg*Cdr1 with functionally assessed ATPase activity, in the apo form and in complex with itraconazole, nucleotides, and vanadate. These structures reveal how the membrane domain of Cdr1 accommodates itraconazole within its drug-binding site (DBS) and how the substrate adapts its conformation to perfectly fit into the site.

The high quality of the accumulated datasets enabled us to explore their structural variability, providing the first experimentally based description of the conformational dynamics following ATP hydrolysis and the alternated access mechanism of the pump at an unprecedented level of detail.

Functional detergent-purified *Cg*Cdr1

We overexpressed *Cg*Cdr1 in *S. cerevisiae* using a previously established expression system that produces a protein conferring full resistance to azole antifungals of the hyper-sensitive yeast host[27]. The protein was harvested as a 20,000 × *g* membrane pellet fraction, referred to hereafter as "C20K," where *Cg*Cdr1 accounted for 4.4 ± 0.2% of the total proteins (Supplementary Figure 2a).

Fifty percent of the ATPase activity in this membrane fraction, insensitive to sodium azide (a mitochondrial F1-ATPase inhibitor), corresponded to approximately 300–400 nmol $Pi \cdot min^{-1} \cdot mg^{-1}$ and was inhibited by nanomolar concentrations of oligomycin[28] or FK506[29], two well-established PDR pump inhibitors (Supplementary Figure 2b). Their effects were not additive, as no further inhibition was observed when both compounds were added simultaneously (Supplementary Figure 2b), confirming that each molecule specifically targets *Cg*Cdr1. Their inhibition constants (*K*i) were estimated to be 110 and 20 nM, respectively (Figure 1d).

This oligomycin/FK506-sensitive ATPase activity of 150–200 $nmol \cdot min^{-1} \cdot mg^{-1}$ of the C20K proteins was therefore attributable to *Cg*Cdr1 (Figure 1d). Considering that 4.4% of C20K fraction was accounted for by *Cg*Cdr1, its specific ATPase activity can be estimated to 3-5 $\mu mol \cdot min^{-1} \cdot mg^{-1}$ (⇔ 1 ATP hydrolyzed/*Cg*Cdr1/100 ms), consistent with previous reports for Pdr5 (2 $\mu mol \cdot min^{-1} \cdot mg^{-1}$)[30]. Measuring ATPase activity with increasing concentrations of itraconazole resulted in a ~30% reduction of the *Cg*Cdr1 specific ATPase activity, with a half maximal effect in the micromolar range (Figure 1d).

*Cg*Cdr1 was extracted from the C20K fraction using a mixture of trans-PCC-α-M (PCC)[31] and dicarboxylate oside 9b (DCOD9b)[32], as previously set up[33]. Subsequent purification steps involving affinity and size-exclusion chromatography yielded a homogeneous protein (Supplementary Figure 2c).

The oligomycin-sensitive ATPase activity of *Cg*Cdr1 in this detergent mixture was of 200 $nmol \cdot min^{-1} \cdot mg^{-1}$. It was completely inhibited by oligomycin and FK506, with a *K*i of 0.7 and 0.1 μM, respectively (Figure 1e). Like its behavior in the C20K membranes, itraconazole induced a limited yet significant reduction of *Cg*Cdr1 ATPase activity with a concentration of half maximal effect of 3.5 μM but still plateauing at 75% beyond 10 μM (Figure 1e). This reduction may reflect a slower translocation process due to the substrate size, as also previously reported[34,35].

The affinity of the purified protein for itraconazole was estimated at a K_D of 0.4 μM (Figure 1f). These biochemical characterizations confirm that *Cg*Cdr1 retains its functionality in the PCC-DCOD9b environment, and that it is amenable to structural studies.

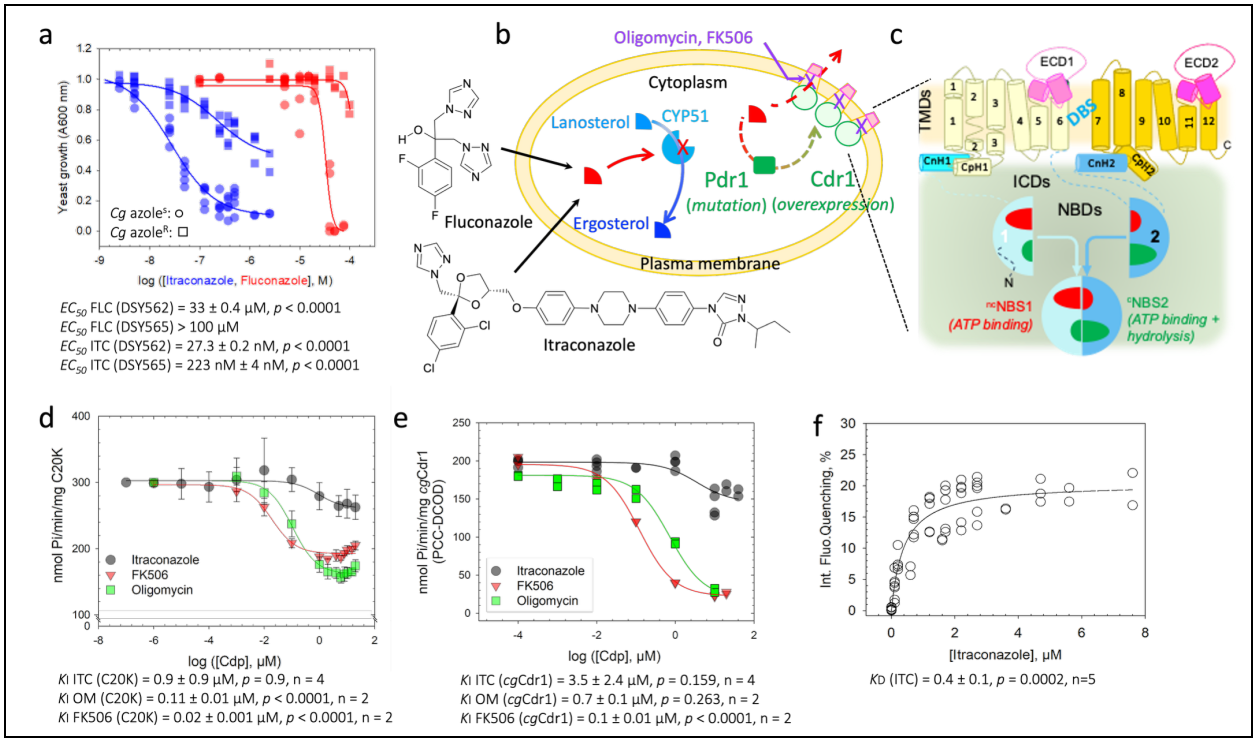

Figure 1. Phenotype and mechanism of azole antifungals resistance. a. Fluconazole and itraconazole resistance patterns of *C. glabrata* clinical isolates. Azole-sensitive (DSY562, circles) and azole-resistant (DSY565, overexpressing *Cg*Cdr1, squares) strains were exposed to increasing concentrations of fluconazole (red) or itraconazole (blue); $n = 5$. **b.** Mechanism of Cdr1 overexpression induced by azole antifungals stress. In response to Cyp51 inhibition by azoles, yeast cells upregulate Cdr1 expression by approximately ten-fold through mutations of the zinc-cluster transcription factor, Pdr1, enhancing the efflux of azoles. This process can be blocked by laboratory inhibitors such as oligomycin or FK506. **c.** Cdr1 topology. Cdr1 consists of extracellular (ECDs), transmembrane (TMDs), intracellular (ICDs), and nucleotide-binding domains (NBDs). When assembled, NBD-1 and NBD-2 form two nucleotide-binding sites: a catalytic site (NBS-1, dark green) that hydrolyzes ATP and a non-catalytic site (NBS-2, red). Drugs bind to the drug-binding site (DBS) and translocate through the TMD into the cell exterior. Structural and functional coupling of the NBDs with the TMDs is mediated by connecting helices (CnH-1, CnH-2) and coupling helices (CpH-1, CpH-2). **d-e.** ATPase sensitivity to inhibitors and substrates of *Cg*Cdr1 in C20K membranes purified with PCC-DCOD9b**. f.** Itraconazole binding to *Cg*Cdr1 measured by intrinsic fluorescence quenching.

High resolution cryo-EM structures of *Cg*Cdr1

We routinely conducted cryo-EM experiments with the protein concentrated to approximately 20 µM (~7 g/L). *Cg*Cdr1 particles were imaged in purified, ligand-free form, representing the apo state. Next, *Cg*Cdr1 was analyzed under turnover conditions by incubating it with 5 mM ATP-Mg^{2+} for 30 minutes at 4 °C, followed by the addition of 1 mM orthovanadate for a further 20 minutes. Vanadate, in its inorganic form (Vi), replaces the inorganic phosphate (Pi) generated by ATP hydrolysis, forming a stable ADP-VO_4^{2-}-Mg^{2+} complex that mimics the ADP-PO_4^{2-}-Mg^{2+} complex[26,36]. Additionally, *Cg*Cdr1 was also incubated under the same conditions in the presence of 30 µM itraconazole.

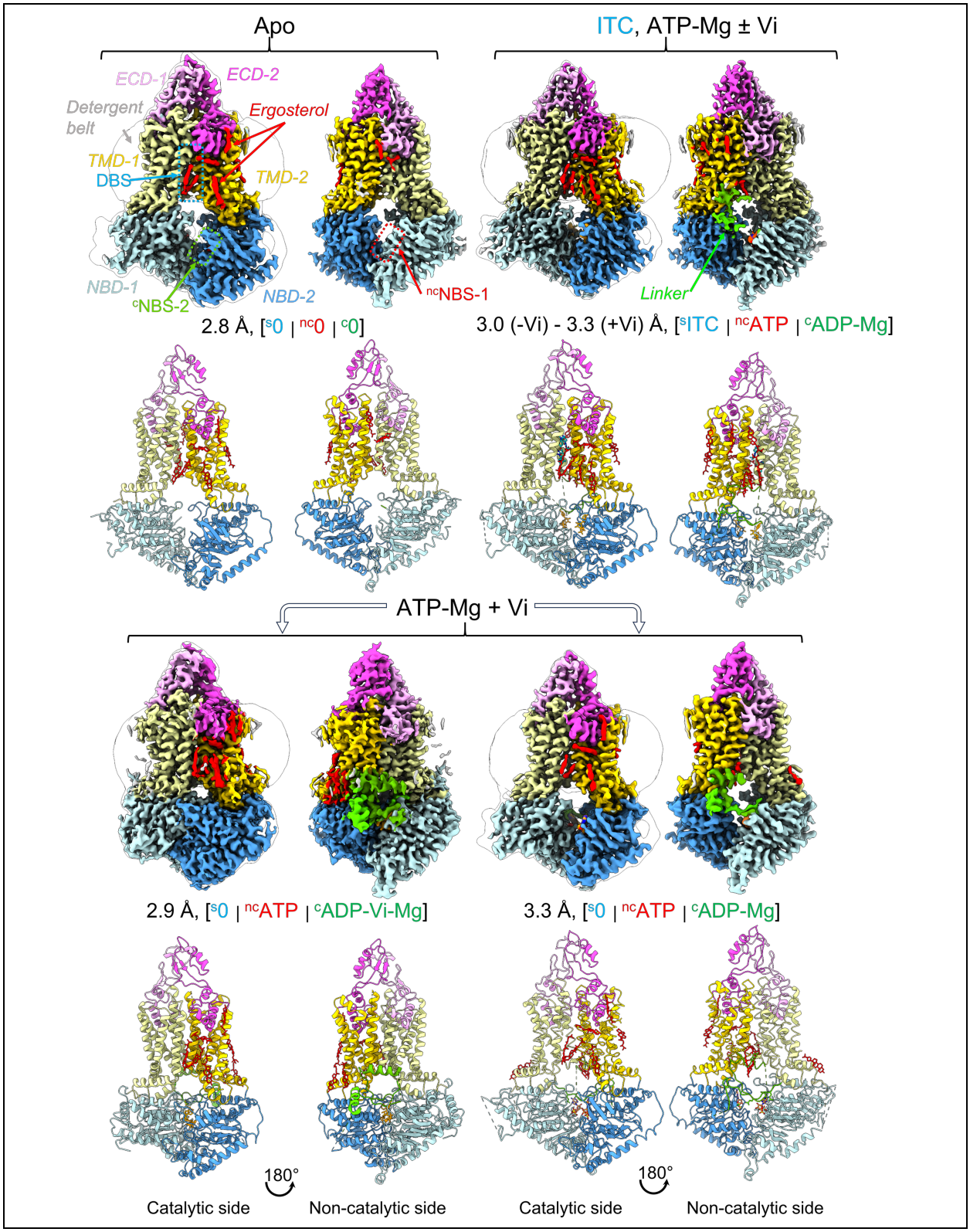

Figure 2. Cryo-EM maps and corresponding 3D models of *Cg*Cdr1. Density maps and their corresponding models, of *Cg*Cdr1 incubated under various conditions. Upper left panel: apo, *i.e.*, nothing

added or found bound after purification either to the DBS (^{s}X), the ^{nc}NBS or the ^{c}NBS (^{nc}X, ^{c}X), [^{s}0|^{nc}0|^{c}0] (contour 0.087). Upper right panel: *Cg*Cdr1 pre-incubated with itraconazole and ATP-Mg^{2+}, with and without vanadate led to the same [^{s}ITC|^{nc}ATP|^{c}ADP-Mg] state (contour 0.065). Lower panels: *Cg*Cdr1 pre-incubated with ATP-Mg^{2+} and vanadate led to 2 major states, [^{s}0|^{nc}ATP|^{c}ADP-Vi-Mg] (contour 0.371) and [^{s}0|^{nc}ATP|^{c}ADP-Mg] (contour 0.34). Catalytic (front view) and non-catalytic faces (rear view) of the protein are shown side by side. The different domains are colored as indicated at the top left. Densities corresponding to ergosterol are shown in red. The density corresponding to the detergent belt surrounding the membrane region is shown as a Gaussian-filtered (2σ) version of the same map.

The final density maps and their corresponding models are presented Figure 2. The loading status of the different binding sites in *Cg*Cdr1 is denoted as [^{s}X|^{nc}X|^{c}X], where *s* represents the substrate bound to the DBS, while *nc* and *c* indicate nucleotides bound to the ^{nc}NBS and ^{c}NBS, respectively. The apo *Cg*Cdr1 produced a density map with a resolution of 2.8 Å (Supplementary Figure 3). The *Cg*Cdr1 samples incubated with itraconazole and ATP-Mg^{2+}, with or without vanadate; generated density maps resolved at 3.3 Å (Supplementary Figure 4) and 2.7 Å (Supplementary Figure 5), respectively. The sample incubated with ATP-Mg^{2+} and vanadate resulted in two distinct maps at 2.9 Å and 3.3 Å (Supplementary Figure 6).

Ergosterols at *Cg*Cdr1 membrane sites

A common feature across these density maps is the presence of multiple densities into which ergosterol molecules fit well (colored in red in Figure 2). We identified by MS/MS 11 ergosterol molecules and the equivalent of one phosphatidylethanolamine (PE)-type and one phosphatidylcholine (PC)-type lipid (Supplementary Figure 7). Although the densities of the PE- and PC-type lipids could not be unambiguously identified in the Cryo-EM structures, ten ergosterol molecules were clearly resolved and labeled Erg-1 to Erg-10 (Supplementary Figure 8a).

The distribution of the ergosterol molecules is asymmetric, with most of them (Erg-1 to Erg-6) binding to the catalytic face of the protein (Figure 3). Erg-1 binds within a cavity capped by hydrophobic residues F1370, W1371, F1373, M1374, and V1377 of helix H-38 in ECD-2, and is stabilized laterally by Y1325 and L1329 of TMH-10, M1350 and L1353 of TMH-11, and Y1472 and F1475 of TMH-12 (Supplementary Figure 8b). Erg-2 binds near the cytoplasmic side of TMD2, along TMH-10. Erg-3 is located within a groove between TMHs -9, -10 and -12, in the center of the membrane bilayer. Erg-4 and Erg-5 are also positioned near the center of the membrane bilayer, between TMH-1 and TMH-11, facing the entrance of the DBS (Supplementary Figure 8b).

Noteworthy, *Ca*Cdr1 has been demonstrated to transport steroid hormones[37]. Several of the residues mentioned above were previously identified as key residues involved in steroid hormone transport by *Ca*Cdr1, specifically interacting with β-estradiol and corticosterone[37,38] (Supplementary Figure 8c). For instance, the Y1328A mutation in *Ca*Cdr1 (Y1325 in *Cg*Cdr1) altered β-estradiol transport, while the M1332A (L1329 in *Cg*Cdr1) and M1356A (L1353 in *Cg*Cdr1) mutations reduced corticosterone transport, consistent with our previous findings that the majority of residues critical for steroid hormone transport were located in TMH-10 and -11[37]. Like Erg-1, several other ergosterol-interacting sites have also been implicated in β-estradiol and/or corticosterone transport. Notably, L663 in *Ca*Cdr1 which corresponds to the Erg10

interacting residue L662 in *Cg*Cdr1, is essential for the transport of both β-estradiol and corticosterone[37].

The mobility of these ergosterol molecules was further evaluated by molecular dynamics simulations of *Cg*Cdr1 placed into a lipid bilayer which revealed poor mobility of these molecules (Supplementary Figure 8d) suggesting an important role of these ergosterol molecules for the integrity of the pump.

The reason for this asymmetric distribution is unclear and warrants further investigation. One plausible mechanical hypothesis is that this distribution reinforces the rigidity of the TMD-2, creating a structural anchor relative for TMD-1. An alternative hypothesis may also be that *Cg*Cdr1 facilitates the translocation of ergosterol from the inner leaflet (Erg-2) to the outer leaflet (Erg-6) through an intermediate location (Erg-1); reminiscent of the "credit card swipe mechanism" described for the transport of phosphatidylcholine-type lipids by human ABCB4[39].

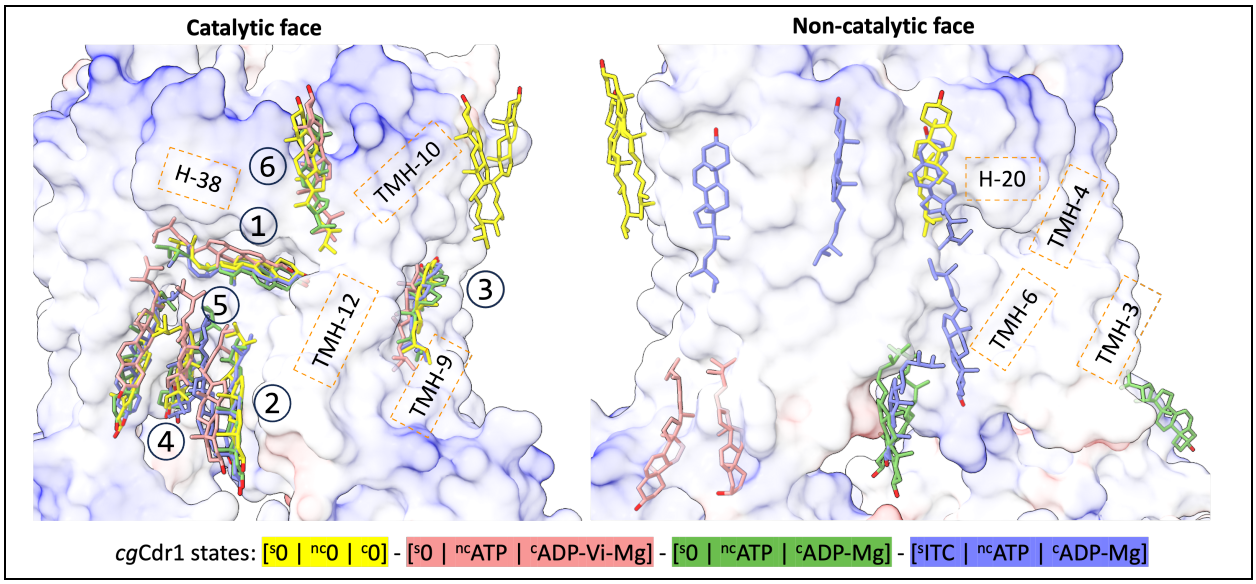

Figure 3. Location of endogenous ergosterol molecules bound to the TMD of *Cg*Cdr1. The TMD regions of the four states of *Cg*Cdr1 are superposed, with views of the catalytic (left) and non-catalytic (right) sides of the TMD. Ergosterol molecules are numbered and color-coded according to the state of *Cg*Cdr1 indicated below, with the apo state surface displayed as a reference.

Type-V apo *Cg*Cdr1 shows no motion

The structure of *Cg*Cdr1 closely resembles that of Pdr5, confirming a general fold for fungal PDR transporters. A detailed view of the protein is displayed in Supplementary Figure 9 (with itraconazole in the DBS). The protein displays a pseudo dimeric organization, with each half containing a NBD, a TMD, and one ECD (Figure 2). In the nucleotide-bound structures, a linker domain is observed near the ^{nc}NBS (colored in green in (Figure 2, viewed from the non-catalytic side). This domain comprises a short *N*-terminal segment (residues 124–151) and the stretch connecting TMH-6 to NBD-2 (residues 788–847). Initially identified in Pdr5, this structural

feature is a hallmark of PDR transporters and is mainly observed in closed-NBDs forms. Conversely, in the apo-state structure, neither of the linker domains is formed due to the absence of nucleotides, preventing domain dimerization. The TMDs are organized into six-helix bundles that provide a pathway for substrates into the extracellular space. TMH-5 and TMH-11 connect to two helical regions, bent at a 90° angle and form two short amphipathic helices (H-20 and H-38 in Supplementary Figure 1c) at the extracellular water-membrane bilayer interface. Between these helices and TMH-6 and TMH-12 are two large ECDs that are much larger than in human type-V ABC transporters. As in Pdr5, the *N*-terminal and *C*-terminal halves of these two ECD are stabilized by one and two disulfide-bonds, respectively.

We investigated the conformational landscape of *Cg*Cdr1 in the apo state by inter-particle variability analysis using the 3DVA in CryoSPARC. Twenty density maps were generated and ordered along a progression of variability that reflects a continuous and sequential conformational pathway. The corresponding 20 three-dimensional structures were then individually refined using the *phenix.varref* tool previously developed[40]. The resulting maps and models (Supplementary Table 2) were combined to generate the animation shown in Supplementary Movie 1. The 3D-models enabled the determination of the displacement for each Cα atom of each frame relative to frame 1 (RMSD), which was helpful in investigating global and local protein movements Supplementary Figure 10, Extended data 1). The overall process shows that *Cg*Cdr1 in this apo state exhibited minimal global and local dynamics, with an overall RMSD of 1.9 Å mostly reflecting local vibrations showing that *Cg*Cdr1 is clearly at rest.

Itraconazole folds in DBS, stabilizes inward

Binding of itraconazole to the DBS of *Cg*Cdr1 in the presence of ATP-Mg^{2+} froze the transporter in an inward-facing conformation after ATP-hydrolysis and release of Pi (Figure 2). Further refinements identified a density in the crevice between the TMDs into which itraconazole could be fitted (Supplementary Figure 11a, Figure 4a). The presence or absence of vanadate during the pre-incubation period led to the same nucleotide loading state, with densities for ADP-Mg^{2+} in the ^{c}NBS and ATP in the ^{nc}NBS clearly visible (Figure 4a).

The overall structures, in absence or presence of vanadate, are almost identical to the [^{s}0|^{nc}ATP|^{c}ADP-Mg] state with an overall RMSD of 0.5 Å, indicating that itraconazole binding does not induce major conformational changes. As expected from its binding mode (Figure 1f), only one itraconazole molecule fits into the DBS, occupying a space from near the inner leaflet of the membrane bilayer to the upper half of the TMHs that constitute the DBS (Figure 4a).

Itraconazole adopts an n-like conformation with the triazolone ring positioned near the DBS bottom. The bulkier dioxolane, triazole, and dichlorophenyl moieties are arranged in a triskelion-like fashion, oriented towards the entry pathway (Figure 4a). Binding is facilitated by residues of TMHs -1, -2, -5 -8 and -11. The chlorine atom of the dichlorophenyl group forms a halogen bond with the nitrogen atom of N1345. Residue S1348 is close enough to the oxygen atom of the dioxolane to establish a H-bond that may be critical for drug binding. This confirms previous mutation studies of the equivalent residues S1360 in Pdr5 and T1351 in *Ca*Cdr1 that were shown to affect drug binding and efflux pump inhibition by FK506[41-44].

Itraconazole primarily interacts with the protein through hydrophobic and Van der Waals forces (Figure 4a, Supplementary Figure 11b) as reflected by the DBS's composition of mostly aliphatic and aromatic residues: F551, L554, L562, I564, and F565 of TMH-2; L663 and M656 of TMH-5;

V1234 and P1238 of TMH-8; and L1355 of TMH-11. The itraconazole binding pocket also features hydrophilic regions at its periphery (Supplementary Movie 2). Compared to the ligand-free inward-facing structures, there is no significant rearrangement of the side chains of these residues (Supplementary Figure 11a).

Residues F550 and F551 of TMH-2 and F1230 of TMH-8 function as a hydrophobic lid, preventing itraconazole from advancing further toward the ECD, by positioning themselves directly above the piperazine moiety. On the opposite side, the entry pathway is delineated by the lower regions of TMHs -1 and -11, facilitating substrate entry from the membrane. However, in all our inward-facing structures, this pathway is obstructed by F514 and N1345 at the bottom, as well as M522 and T1352 at the upper part of the entry route, with their Cryo-EM densities clearly defined. Perhaps these residues function as a drug entry filter. This hypothesis is strengthened by the spatial vicinity (one helical turn upwards of F514) of a glycine residue, G518. The equivalent residue in *Ca*Cdr1 (G521) was previously identified critical for substrate gating, most likely because it brings the required conformational flexibility to the entry gate[45].

Interestingly, two of the tightly bound ergosterol molecules (Ergs -4 and -5) reside at this entry gate, no matter the conformational state of *Cg*Cdr1 (Figure 3). There is no noticeable exit pathway above the DBS, whatever the state of *Cg*Cdr1, suggesting that all *Cg*Cdr1 structures represent various stages of the transporter with the DBS inaccessible to the extracellular space (Supplementary Figure 11).

During model building, there were noticeable local deformations of TMH-2 and to a lesser extent, TMH-8. Figure 4b shows the unwinding of two helical turns of TMH-2 between residues 559-565 due to a loss of the backbone H-bond between S559 and L562. This unwinding creates space for itraconazole binding and confers different flexibilities to the two halves of the helix: its lower half is positioned parallel to itraconazole, while the upper part leans over the substrate, closing the exit pathway in this inward-facing conformation. TMH-8 also shows a local deformation of residues V1234 to P1238, which generates additional space for itraconazole to bind. (Figure 4a, Supplementary Movie 2). TMH-2 and -8 thus appear to be the key structural elements for accommodating substrates within the DBS. This adaptability of the DBS is also complemented by the ability of the ITC to fold over itself, thus optimizing its spatial occupancy within the site.

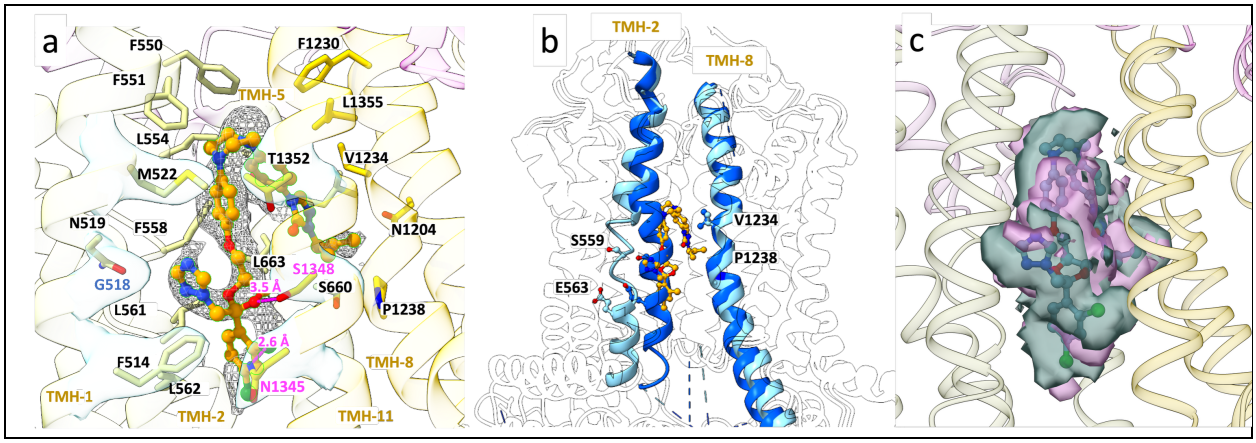

Figure 4. Structural features of the DBS. a. Enlarged itraconazole binding region. Itraconazole is shown in sticks and balls colored by atom type, with carbon in orange. The density map is displayed as a mesh at

a contour level of 0.0318. Potential H-bonds with the indicated distances between itraconazole and residues of the DBS are depicted in magenta dashed-lines. Residues establishing Van der Waals contacts are labeled and shown as sticks. The densities of F514, G518, M522 and N1345, S1348, T1352 delineating the entry path are shown as blue surfaces **b**. Local deformations of TMHs -2 and -8 in the [^{s}0|^{nc}ATP|^{c}ADP-Vi-Mg] and [^{s}ITC|^{nc}ATP|^{c}ADP-Mg] states are colored in dark and light blue, respectively. Boundary residues of the deformations are shown as sticks: S559 and E563 for TMH-2 and V1234 and P1238 for TMH-8. Itraconazole is shown in orange sticks as a reference. **c**. Conformational variability of itraconazole bound to the DBS. Superposition of frame 4 in pink, and frame 16 in dark green. The cartoon model built from the high-resolution structure is shown as a reference, and itraconazole as sticks.

In the [^{s}0|^{nc}ATP|^{c}ADP-Vi-Mg] state, the DBS-forming transmembrane helices have converged into the DBS, occluding it. TMH-2 shows the most impressive displacement, with its lower part 575-550 moving up to 7 Å towards the center the DBS, while the top half remains largely unperturbed, causing straightening and restoration of the alpha-helical conformation of this TM. This dramatic inward movement of the lower part of TMH-2 may force the substrate up and push them through an exit channel into the cell exterior (Figure 4b).

The conformational space variability of *Cg*Cdr1 bound to itraconazole was explored as described above for the apo state using 3DVA and VARREF, generating 20 successive maps and 3D-models (Supplementary Table 2) displayed in Supplementary Figure 12 and assembled in the Supplementary Movie 3. The displacement for each Cα atom of each frame relative to frame 1 was then calculated (Supplementary Figure 12, Extended data 2). *Cg*Cdr1 bound to itraconazole showed minimal global dynamics, close to those of the apo state. However, the itraconazole assumes distinct positions around the same core of the density, particularly clear when superposing frames 1 and 17 (Figure 4c). The relative mobility of itraconazole was not surprising, though, considering the rather hydrophobic environment within the DBS and its role as a transition pathway of drugs rather than a stable drug binding site. This mobility may also explain the rather weaker density observed for the itraconazole compared to the nearby protein.

^{nc}ATP and ^{c}ADP bound to basal *Cg*Cdr1

The apo state structure (Figure 2) revealed no electron density corresponding to any nucleotide in either NBS. The two density maps obtained for *Cg*Cdr1 incubated with ATP-Mg^{2+} and vanadate displayed an ATP molecule without magnesium in the ^{nc}NBS Figure 5a), confirming previous observations made with Pdr5[26]. In contrast, the loading of each ^{c}NBS varied, bound to either an ADP-Vi-Mg^{2+} or an ADP-Mg^{2+} complex. This suggests that the release of vanadate had already occurred in a subset of the particles while vanadate had locked the other population of the protein in a post-hydrolytic state resembling the [^{nc}ATP|^{c}ADP-Pi-Mg] state of the protein before the release of the γ-phosphate and the return of the transporter to its inward-facing conformation.

By contrast, the same cryo-EM investigations of *Cg*Cdr1 incubated with ITC, ATP-Mg^{2+} and vanadate revealed only one structure for *Cg*Cdr1 with ATP bound to the ^{nc}NBS and an ADP-Mg^{2+} complex bound to the ^{c}NBS.

The persistence of an ATP molecule bound to the ^{nc}NBS prompted us to evaluate its affinity to the ^{nc}NBS using an intrinsic fluorescence quenching assay. The data yielded saturation curves that fit well with a single ATP binding site, with a K_D of 0.3 μM (Figure 5b). This K_D was

significantly lower than the 150 μM K_D value previously determined for ATP-Mg^{2+} bound to *Ca*Cdr1[33].

Taken together, these data suggest that under optimal growth conditions, where nutrients are abundant with millimolar intracellular ATP concentrations[46], *Cg*Cdr1 permanently binds ATP at the ^{nc}NBS. These data suggest that the two NBSs display rather different ATP affinities, which is to be expected given their asymmetric nature. However, the permanently bound ^{nc}ATP molecule does not appear to be a true cofactor as it is lost during protein purification.

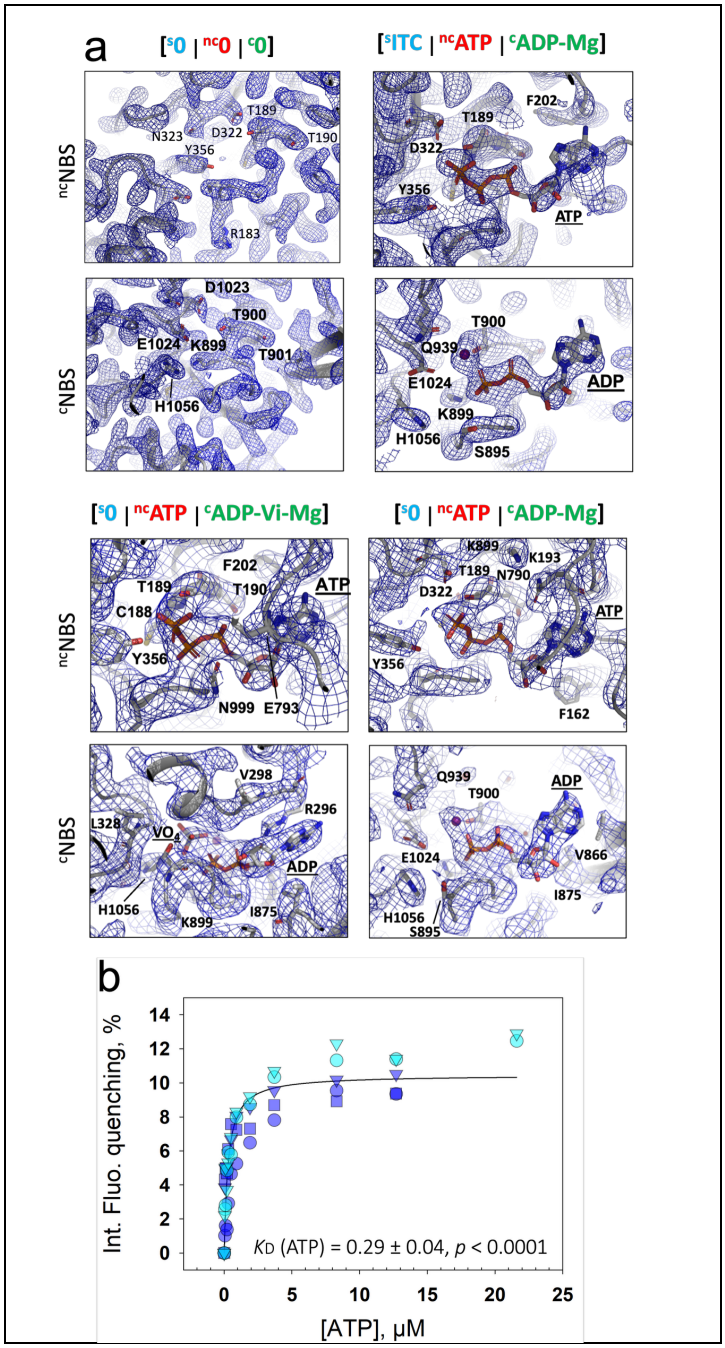

Figure 5. Cryo-EM density map details of the NBSs. a. Coulomb potential maps, at a contour level of 0.1 for [^{s}0|^{nc}0|^{c}0], 0.055 for [^{s}ITC|^{nc}ATP|^{c}ADP-Mg], 0.52 for [^{s}0|^{nc}ATP|^{c}ADP-Vi-Mg], and 0.3 for [^{s}0|^{nc}ATP|^{c}ADP-Mg]. **b.** Binding of ATP to cgCdr1 probed by intrinsic fluorescence quenching performed in two independent biological replicates, in duplicate and triplicate, respectively.

Cryo-EM dynamics of ATP-driven motion

Experimental Set up.

The ability to capture from the same grid two closely related, yet distinct, states of CgCdr1 incubated with nucleotides and vanadate as displayed in Figure 2 provided a unique opportunity to leverage the full potential of inter-particle variability analysis of cryo-EM samples[47]. Cryo-EM data processing including 2D and 3D classifications identified three distinct classes of particles. The two most abundant classes, which gathered 50% and 32% of the particles, corresponded to the closed [^{s}0|^{nc}ATP|^{c}ADP-Vi-Mg] and in the open [^{s}0|^{nc}ATP|^{c}ADP-Mg] states, respectively. The third class of particles displayed an intermediate conformation that could not be resolved at high resolution Supplementary Figure 6).

We aligned all the particles of the most abundant [^{s}0|^{nc}ATP|^{c}ADP-Vi-Mg] state and performed a variability analysis starting from this conformation. The latent coordinate analysis revealed a non-Gaussian particle distribution (Supplementary Figure 13a), forming a non-spherical cloud indicative of the presence of sub-states Supplementary Figure 13b). Crucially, the continuum between these sub-states suggested that the selected particles should enable the capture of transitional conformations.

The latent space was interpreted linearly for components C0 and C1 and explored as described above for the apo state using the 3DVA tool in CryoSPARC, generating 20 sequential maps (frames) for each direction. The resulting density maps were further refined into 3D models using the phenix.varref tool (Supplementary Figure 13c, Supplementary Table 2) that allowed to calculate the RMSD for each Ca atom of each frame relative to frame 1 (Extended data 3 and Extended data 4 for C0 and C1, respectively).

Global and local 1D displacements analyses.

The resulting 3D-models are displayed superposed in Figure 6a, left for particles from Component 0 and right for Component 1. The corresponding animations of frame 1 to frame 20 for each component are shown in Movie 1 (C0) and Movie 2 (C1), As shown, component C0 captured large-scale conformational transitions involving all domains of *Cg*Cdr1 whereas component C1reflected more focused motions of the TMD.

At the domain level (Figure 6b), analysis of the RMSD patterns in dataset C0 (left panel) revealed two groups based on their amplitude of motion: one with large displacements (~3 Å), including the NBDs, the linker, and TMD-1, and another with smaller ones (~2 Å), comprising TMD-2 and the two ECDs. In the NBDs, comprised of the RecA-like (RD) and the helical (HD) subdomains (*49-51*) (see detailed locations in Supplementary Figure 1c), the analysis revealed a particularly large displacement of ~5 Å of HD-1, a critical region for ATP-binding and -hydrolysis at the ^{c}NBS.

At the primary sequence level (Figure 6c), the C0 dataset (upper panel) showed that the conserved NBD motif residues—green for catalytic, red for non-catalytic—remain largely in low-mobility regions, consistent with their nucleotide-binding role. However, the ABC signature motif of NBD-1 and the Walker A motif of NBD-2, which flank each side of the ^{c}NBS, display significantly large displacements from 4 to 6.5 Å, highlighting their critically important contribution in ATP hydrolysis. Several NBD regions are particularly involved here, primarily

the C-helix (H-8) that follows the C-loop of the ABC signature in HD-1 and several regions in RD-2, notably B-14 to B-17 and B-23-B-24 β-sheets, and H-31 to H-34 α-helices.

A closer look at the α-helices of HD-1showed that H-6, H-7 and H-8 (Supplementary Figure 14a) undergo distinct mobilities and timing despite their proximity. Indeed, H-6 and H-7 residues exhibit a mobility range of 2 to 6 Å with an important variability while H-8 residues display a larger but much more synchronized mobility between 5 and 7 Å. Importantly, the movement of H-8 residues begins as early as frame 8, preceding those of H-6 and H-7, which only start after frame 12—suggesting that the H-8 triggers the conformational transition of *Cg*Cdr1 from the outward to the inward facing conformations following ATP hydrolysis.

The relative displacements calculated for individual TMH residues confirm the generally higher mobility of TMD-1 helices compared to those of TMD-2 (Supplementary Figure 14, panels b *vs*. c). TMHs -1, -2, -3, and -6 (panel b) undergo in addition an asymmetric deformation with larger displacements observed for their inner compared to the outer leaflet counterparts. As described above for H-6 and H-7, the displacement of these TMD-1 helices starts after frame 12, highlighting the earlier motion of the H-8 in the overall transition.

The same analysis of the C1 data set (Figure 6) showed significant, yet lower mobility of the protein compared to C0 class of particles. Each of the domains moves relatively little, capping at a maximum of 2 Å (panel c, right). However, this class of particles highlights a motion within TMD-1, particularly significant motions of TMH-2 and TMH-5 with high mobilities observed for the segments embedded in the inner leaflet of the bilayer, shifting by up to 4–5 Å each (Supplementary Figure 15).

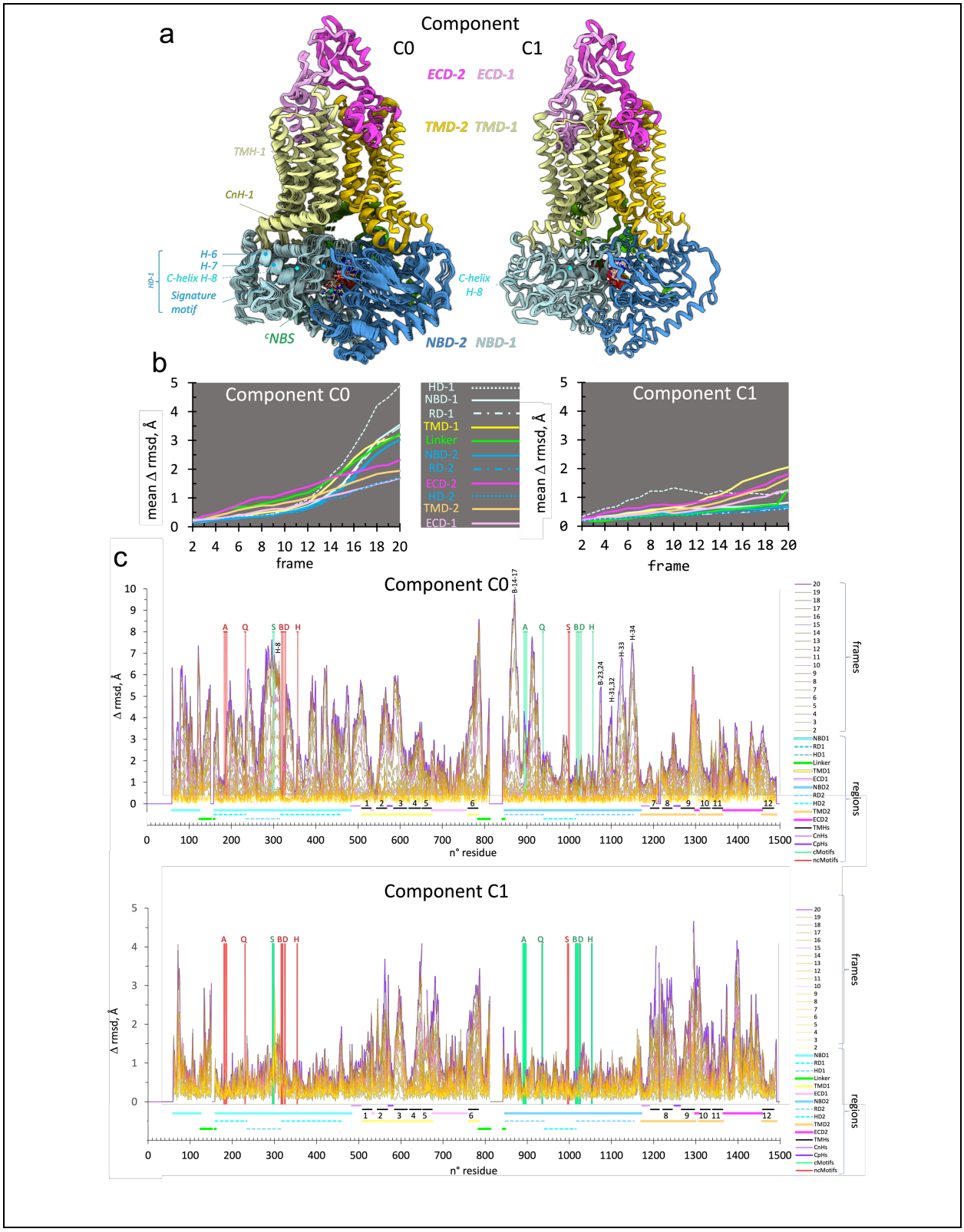

Figure 6. Conformational variability analysis of the transition from the closed [^{s}0|^{nc}ATP|^{c}ADP-Vi-Mg] to the open [^{s}0|^{nc}ATP|^{c}ADP-Mg] states of *Cg*Cdr1 of component C0 and C1 particles. a.

Superposition of the 3D-models of the 20 frames of component C0 (left) and C1 (right) particles. The pictures show the projected movements of the transporter viewed from the catalytic side at the front of the transporter. **b.** Plots of mean Cα RMSD of frames 2 to 20 *vs* frame 1 for each of the indicated regions of component C0 (left) and C1 (right) particles. Regions are colored as in panels a, b and Figure 2. the 'helical' and 'RecA' sub-domains, HD and RD, of each NBD are also included. **c.** Plots of Cα RMSD per residue of frames 2 to 20 *vs* frame 1 of component C0 (top) and C1 (bottom) particles. Plots are superposed from frame 2 at the bottom to frame 20 at the top. The traces from 2 to 19 are colored with a gradient from yellow to brown; traces 10, 15, and 20 are colored with a gradient from pink to purple. The positions of the different domains are indicated below the graph and the positions of the various catalytic and non-catalytic motifs, colored in green and red, respectively, are displayed directly on the graph. A, B: Walker A, B, S: signature motif, Q, D, and H: Q, D, and H loops (see detailed locations in Supplementary Figure 1c). The indicated sheets (B-x) and helices (H-x) are commented on in the text.

Global and local 3D displacements analyses.

Movie 1 reveals how the opening of *Cg*Cdr1 triggered by ATP hydrolysis is rooted along a vertical axis normal to the membrane plane passing through the ATP permanently bound to the ^{nc}NBS. The movements of important regions in terms of angles and distances are detailed in Figure 7. The stability of these movements is provided by TMD-2 with an overall vibration of no more than 2 Å (Figure 6b). Similarly, the ^{nc}NBS, positioned directly underneath TMD-2 also barely moves (Figure 7a, lower right panel). However, the part of NBD-2 containing the catalytic Walker A and B motifs and binding ^{c}ADP-Vi-Mg^{2+} translates away from NBD-1 by ~4-5 Å (Figure 7a, lower right panel). The transition from the closed to the open conformations of NBD-1 causes a rotation of the entire domain by ~10° centered at the β-sheet B-8 residue T352 (Figure 7a, lower left panel). This rotation translates to TMD-1 with the same amplitude and centered at TMH-5 that is in contact with TMD-2 and thus doesn't move much (Figure 7a, upper left panel). The rotation is visible on all TMHs and depicted for TMH-1 and TMH-3 (Figure 7a, upper left panel). TMH-2, however, undergoes unique movements by partially unfolding of the lower half of the helix (F558-I573), as described above (Figure 7a, upper left panel).

A pivotal role for C-helix H-8, triggering large conformational changes of CgCdr1 in response to ATP hydrolysis.

A key feature highlighted by the variability analysis described above is the dramatic displacement of the C-helix H-8 of the ^{c}NBS. In the [^{s}0|^{nc}ATP|^{c}ADP-Vi-Mg] state, the *N*-terminal region of H-8 initially establishes H-bonds with the vanadate with G300 and G301 that are part of the 'VSGG' signature motif of the ABC transporter defining C-loop, and then moves away from the vanadate by a translation of 3.8 Å towards the back of the domain in a piston-like motion (Figure 7b, Frames 1-14). During the duration of this movement, the rest of the domain moves a lot less. A second type of movement is then observed (Figure 7b, Frames 15-20) where the C-helix undergoes a 9.5° rotation around T352, matching the ~10˚ rotation mentioned above for the rest of NBD-1 and parts of TMD-1. Helix H-8 thus undergoes two distinct motions while moving away from the ADP-Vi-Mg^{2+} complex in a movement intimately linked to ATP hydrolysis. This piston-like movement is enabled by a cavity at its *C*-terminus (Figure 7c left panel), observed in the closed conformation of *Cg*Cdr1 in complex with ADP-Vi-Mg^{2+} and not present in the inward-facing conformation of *Cg*Cdr1 in complex with ADP-Mg^{2+} (Figure 7c left *vs* right panels). This initial piston-like motion precedes the domain-scale rearrangements following ATP hydrolysis.

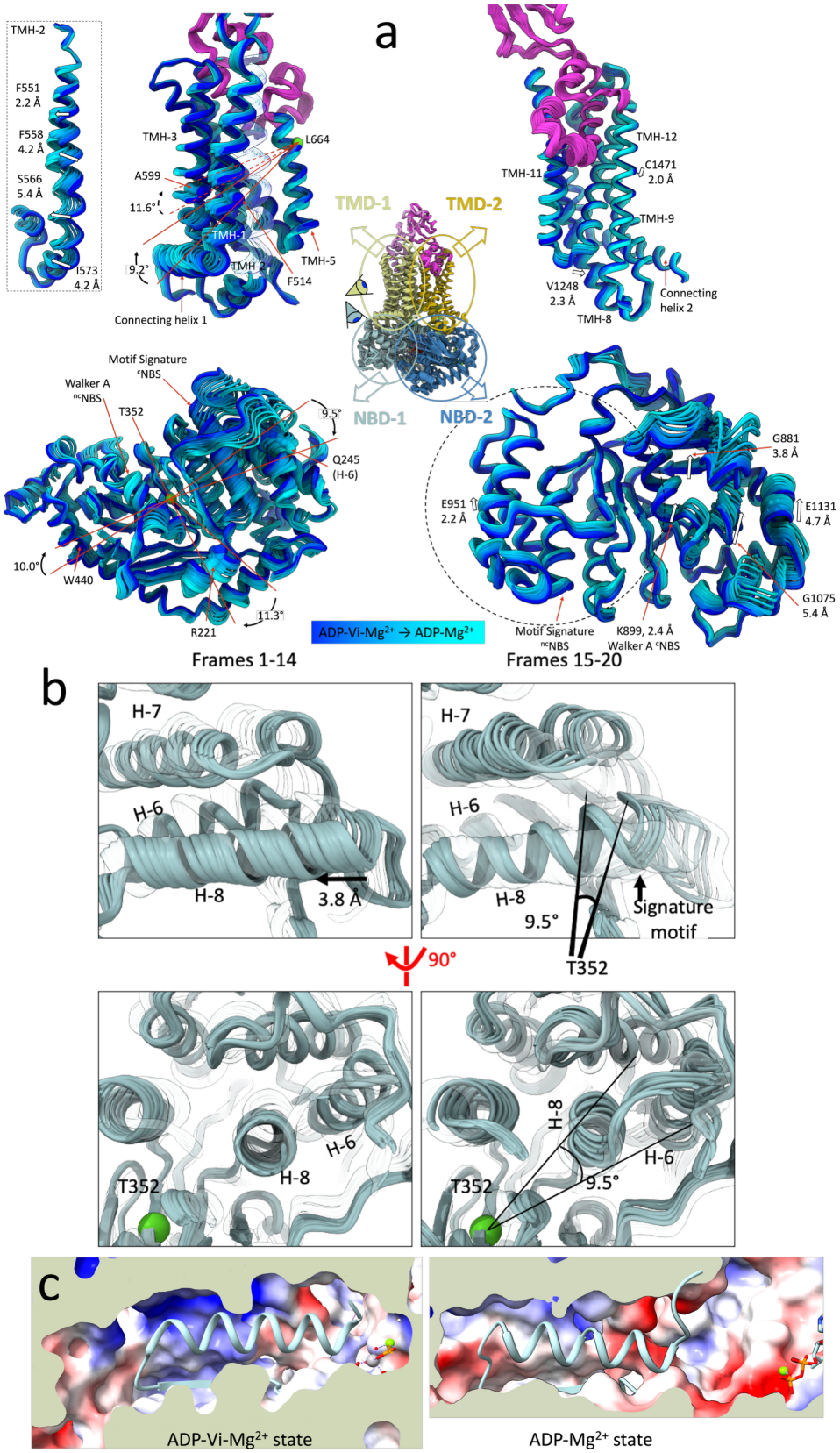
a
TMH-2
F551
2.2 Å
F558
4.2 Å
S566
5.4 Å
I573
4.2 Å
TMH-3
L664
A599
11.6°
TMH-1
9.2°
TMH-2
TMH-5
F514
Connecting helix 1
TMD-1
TMD-2
NBD-1
NBD-2
TMH-12
TMH-11
C1471
2.0 Å
TMH-9
V1248
2.3 Å
TMH-8
Connecting
helix 2
Motif Signature
cNBS
Walker A
ncNBS
T352
9.5°
Q245
(H-6)
10.0°
W440
R221
11.3°
ADP-Vi-Mg2+ → ADP-Mg2+
Frames 1-14
Frames 15-20
G881
3.8 Å
E951
2.2 Å
E1131
4.7 Å
G1075
5.4 Å
Motif Signature
ncNBS
K899, 2.4 Å
Walker A cNBS
b
H-7
H-6
H-8
3.8 Å
9.5°
Signature
motif
90°
T352
H-8
H-6
T352
c
ADP-Vi-Mg2+ state
ADP-Mg2+ state

Figure 7. Three-dimensional transition from the [^{s}0|^{nc}ATP|^{c}ADP-Vi-Mg] to the [^{s}0|^{nc}ATP|^{c}ADP-Mg] states of *Cg*Cdr1 triggered by a piston-like motion of the C-helix H-8 connected to the C-loop of HD-1. a. Projected 3D-motions of the NBD and TMD regions of Component C0 particles of *Cg*Cdr1. The structure is shown in cartoon colored from blue to cyan to depict the transition across the different models. TMH-2 is represented transparent in the whole TMD-1 image and independently in the frame next to it, as its movement is different from the rest of the TMD-1. Movements are listed for each domain with white arrows showing the directionality and amplitude listed. **b.** HD-1 subdomain and C-helix H-8 piston-like motions. Cdr1 is in cartoon colored in light green as NBD-1 in Figure 2, with on the left side the frames 1-14 in solid color and the rest transparent while on the right side the frames 1-14 are transparent and 15-20 are in solid color. The bottom panel shows the same representation turned 90°. Helices are labeled on the image for clarity. Frames 1-14 show a piston-like movement of the C-helix in the plane of the helix, while frames 15-20 show a further displacement out of plane that is a rotation of 9.5° based on T352 position, following the movement of the domain. **c.** Slice view of the C-helix shown in cartoon and the rest of the domain in electrostatic surface potential shown for the surrounding region. In the ADP-Vi-Mg^{2+} state, the *N*-terminus of the C-helix is coordinating the γ-phosphate leaving a cavity at its *C*-terminus. In the ADP-Mg^{2+} state, the C-helix has moved backwards into this cavity, filling-up the void.

Local constrictions of the transmembrane domains squeeze the drug-binding site

Contrary to the global movements revealed by the variability analysis of C0 particles (Figure 6a left, Movie 1), C1 particles show a constriction-like movement of certain TMHs of TMD-1 towards the center of the DBS (Figure 6a right, Movie 2) while *Cg*Cdr1 remains in the [^{s}0|^{nc}ATP|^{c}ADP-Vi-Mg] state during all stages of this locally constricted motion. But even in this conformational ensemble no exit pathway was visible.

The analysis revealed that TMHs -3, -4 and -6 collapses towards TMHs -2 and -5 while the coupling helix CpH-1 between TMHs -2 and -3 moves upwards and stretches between residues F565 and A570, conferring a spring-like motion to the rest of TMH-2, which compresses and moves upwards. A similar motion is also carried out by TMH-5. In TMD-2, the central part of TMH-8 (F1230-S1246) collapses into the DBS, with TMHs -9 and -10 moving as a rigid body and pivoting towards the center of the TMDs (Supplementary Figure 16). While the absence of the substrate and an exit pathway does not allow us to unambiguously attribute this movement to a certain stage of the transport cycle, we think that this 'squeeze and push' movement may play a role in substrate translocation, forcing the substrate through a hydrophobic exit valve[48] above the DBS and pushing the substrate through the ECD into the cell exterior.

Model for the transport cycle of *Cg*Cdr1

The present *Cg*Cdr1 structures and the 3D variability analyses enabled us to visualize incremental steps of the large conformational changes experienced by the transporter during ATP-hydrolysis and the release of Pi. They allow to propose the model displayed in Figure 8 for the transport cycle of *Cg*Cdr1. In the absence of ATP-Mg in the ^{c}NBS, the protein adopts an inward-facing conformation, represented by the [^{s}0|^{nc}0|^{c}0] and the [^{s}0|^{nc}ATP|^{c}ADP-Mg] structures. At this stage of the transport cycle the DBS is open towards the cytoplasm and accessible to substrates. This state, depicted by the [^{s}ITC|^{nc}ATP|^{c}ADP-Mg] structure, shows that substrate binding does not induce any conformational change, suggesting that it resides rather than tightly binds into the DBS, which may partially explain its polyspecificity. Binding of ATP at the ^{c}NBS switches the

transporter into the closed conformation, with the TMHs collapsing into the DBS and forcing substrate transport into the extracellular space by a 'squeeze and push' movement, as depicted in the 3DVA of C1 particles for the [^{s}0|^{nc}ATP|^{c}ADP-Mg] bound state. ATP hydrolysis is necessary to return the protein to its resting [^{s}0|^{nc}ATP|^{c}ADP-Mg] conformation, ready for a new transport cycle. The 3DVA of C0 particles describes this movement in detail, identifying in NBD-1 the ABC signature motif and its vicinal C-helix as structural triggers for the opening of the transporter. The present data also reveal that ATP remains bound to the ^{nc}NBS throughout the transport cycle, with the site, locked by the linker domain, acting as a pivot for domain rotation. This is further supported by its high affinity ($K_D \approx 0.3$ µM) for ATP, showing that the two NBSs have distinct roles necessary for substrate transport across the cell membrane.

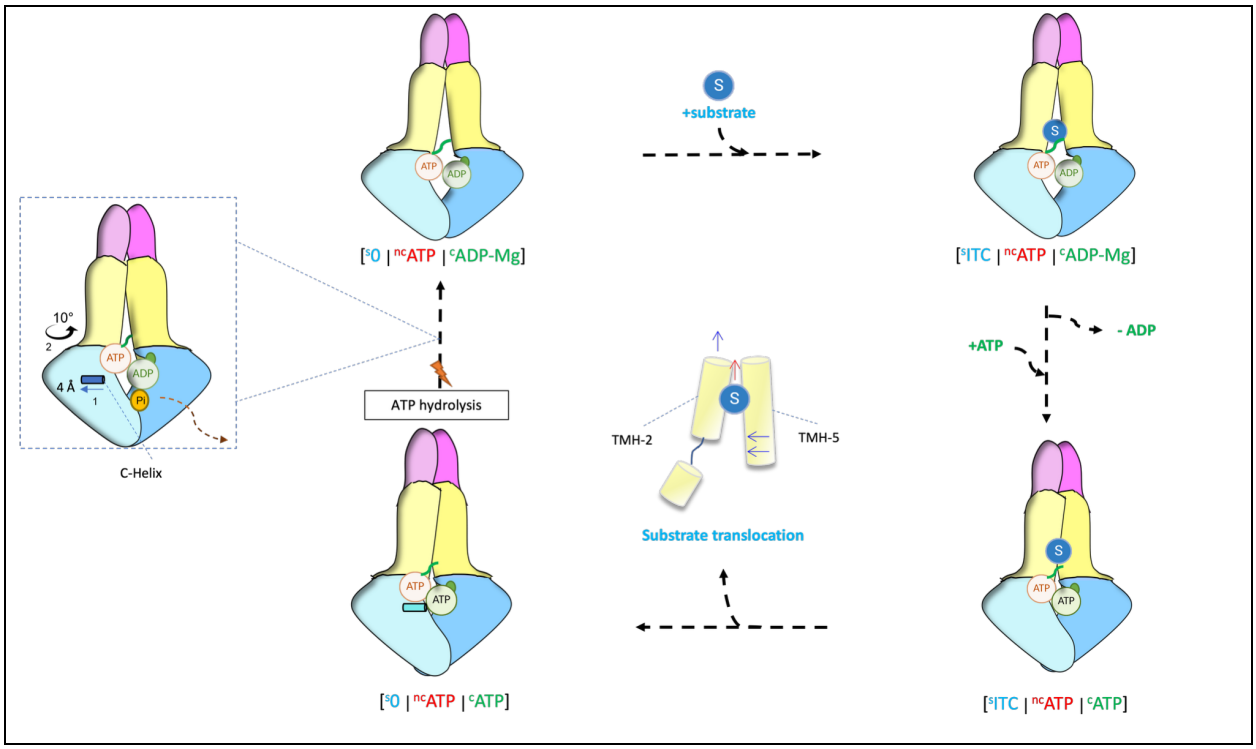

Figure 8. Proposed transport model for *Cg*Cdr1. NBDs -1 and -2 are depicted in light blue and blue, TMDs -1 and -2 in pale yellow and yellow, ECDs -1 and -2 in rose and purple and the linker is in green. The substrate translocation step shows the movement of TMHs -2 and -5 in component C1 of the [^{s}0|^{nc}ATP|^{c}ADP-Vi-Mg] dataset. ATP hydrolysis triggers the backward movement of the C-helix that dissociates the ^{c}NBS.

Methods

Methods are detailed in the Supplementary Information section.

References

1 Denning, D. W. Global incidence and mortality of severe fungal disease. *The Lancet Infectious Diseases* **24**, e428-e438 (2024). https://doi.org:10.1016/S1473-3099(23)00692-8

2 Stop neglecting fungi. *Nat Microbiol* **2**, 17120 (2017). https://doi.org:10.1038/nmicrobiol.2017.120

3 Hoenigl, M. *et al.* COVID-19-associated fungal infections. *Nat Microbiol* **7**, 1127-1140 (2022). https://doi.org:10.1038/s41564-022-01172-2

4 Bolotin-Fukuhara, M. & Fairhead, C. *Candida glabrata*: a deadly companion? *Yeast* **31**, 279-288 (2014). https://doi.org:10.1002/yea.3019

5 Du, H. *et al. Candida auris*: Epidemiology, biology, antifungal resistance, and virulence. *PLoS Pathog* **16**, e1008921 (2020). https://doi.org:10.1371/journal.ppat.1008921

6 Drouhet, E. & Dupont, B. Evolution of antifungal agents: past, present, and future. *Rev Infect Dis* **9 Suppl 1**, S4-14 (1987). https://doi.org:10.1093/clinids/9.supplement_1.s4

7 Campoy, S. & Adrio, J. L. Antifungals. *Biochem Pharmacol* **133**, 86-96 (2017). https://doi.org:10.1016/j.bcp.2016.11.019

8 Jorgensen, L. N. & Heick, T. M. Azole Use in Agriculture, Horticulture, and Wood Preservation - Is It Indispensable? *Front Cell Infect Microbiol* **11**, 730297 (2021). https://doi.org:10.3389/fcimb.2021.730297

9 Monk, B. C. *et al.* Fungal Lanosterol 14alpha-demethylase: A target for next-generation antifungal design. *Biochim Biophys Acta Proteins Proteom* **1868**, 140206 (2020). https://doi.org:10.1016/j.bbapap.2019.02.008

10 van Meer, G., Voelker, D. R. & Feigenson, G. W. Membrane lipids: where they are and how they behave. *Nat Rev Mol Cell Biol* **9**, 112-124 (2008). https://doi.org:10.1038/nrm2330

11 Cannon, R. D., Fischer, F. J., Niimi, K., Niimi, M. & Arisawa, M. Drug pumping mechanisms in *Candida albicans*. *Nihon Ishinkin Gakkai Zasshi* **39**, 73-78 (1998). https://doi.org:10.3314/jjmm.39.73

12 Prasad, R. & Kapoor, K. Multidrug resistance in yeast *Candida*. *Int Rev Cytol* **242**, 215-248 (2005). https://doi.org:10.1016/S0074-7696(04)42005-1

13 Decottignies, A. & Goffeau, A. Complete inventory of the yeast ABC proteins. *Nat Genet* **15**, 137-145 (1997). https://doi.org:10.1038/ng0297-137

14 Gaur, M., Choudhury, D. & Prasad, R. Complete inventory of ABC proteins in human pathogenic yeast, *Candida albicans*. *J Mol Microbiol Biotechnol* **9**, 3-15 (2005). https://doi.org:10.1159/000088141

15 Kumari, S. *et al.* ABC transportome inventory of human pathogenic yeast *Candida glabrata*: Phylogenetic and expression analysis. *PLoS One* **13**, e0202993 (2018). https://doi.org:10.1371/journal.pone.0202993

16 Ferrari, S. *et al.* Gain of function mutations in CgPDR1 of *Candida glabrata* not only mediate antifungal resistance but also enhance virulence. *PLoS Pathog* **5**, e1000268 (2009). https://doi.org:10.1371/journal.ppat.1000268

17 Balzi, E. & Goffeau, A. Multiple or pleiotropic drug resistance in yeast. *Biochim Biophys Acta* **1073**, 241-252 (1991). https://doi.org:10.1016/0304-4165(91)90128-4

18 Thomas, C. *et al.* Structural and functional diversity calls for a new classification of ABC transporters. *FEBS Lett* **594**, 3767-3775 (2020). https://doi.org:10.1002/1873-3468.13935

19 Moreno, A., Banerjee, A., Prasad, R. & Falson, P. PDR-like ABC systems in pathogenic fungi. *Res Microbiol* **170**, 417-425 (2019). https://doi.org:10.1016/j.resmic.2019.09.002

20 Banerjee, A., Moreno, A., Pata, J., Falson, P. & Prasad, R. ABCG: a new fold of ABC exporters and a whole new bag of riddles! *Adv Protein Chem Struct Biol* **123**, 163-191 (2021). https://doi.org:10.1016/bs.apcsb.2020.09.006

21 Banerjee, A. *et al.* Structure, function, and inhibition of catalytically asymmetric ABC transporters: Lessons from the PDR subfamily. *Drug Resist Updat* **71**, 100992 (2023). https://doi.org:10.1016/j.drup.2023.100992

22 Sauna, Z. E. *et al.* Mutations define cross-talk between the N-terminal nucleotide-binding domain and transmembrane helix-2 of the yeast multidrug transporter Pdr5: possible conservation of a signaling interface for coupling ATP hydrolysis to drug transport. *J Biol Chem* **283**, 35010-35022 (2008). https://doi.org:10.1074/jbc.M806446200

23 Downes, M. T. *et al.* The transmission interface of the Saccharomyces cerevisiae multidrug transporter Pdr5: Val-656 located in intracellular loop 2 plays a major role in drug resistance. *Antimicrob Agents Chemother* **57**, 1025-1034 (2013). https://doi.org:10.1128/aac.02133-12

24 Banerjee, A. *et al.* Cdr1p highlights the role of the non-hydrolytic ATP-binding site in driving drug translocation in asymmetric ABC pumps. *Biochim Biophys Acta Biomembr* **1862**, 183131 (2020). https://doi.org:10.1016/j.bbamem.2019.183131

25 Banerjee, A. *et al.* W1038 near D-loop of NBD2 is a focal point for inter-domain communication in multidrug transporter Cdr1 of *Candida albicans*. *Biochim Biophys Acta Biomembr* **1860**, 965-972 (2018). https://doi.org:10.1016/j.bbamem.2018.01.022

26 Harris, A. *et al.* Structure and efflux mechanism of the yeast pleiotropic drug resistance transporter Pdr5. *Nat Commun* **12**, 5254 (2021). https://doi.org:10.1038/s41467-021-25574-8

27 Lamping, E. *et al.* Characterization of three classes of membrane proteins involved in fungal azole resistance by functional hyperexpression in Saccharomyces cerevisiae. *Eukaryot Cell* **6**, 1150-1165 (2007). https://doi.org:10.1128/ec.00091-07

28 Decottignies, A., Kolaczkowski, M., Balzi, E. & Goffeau, A. Solubilization and characterization of the overexpressed PDR5 multidrug resistance nucleotide triphosphatase of yeast. *J Biol Chem* **269**, 12797-12803 (1994).

29 Kralli, A. & Yamamoto, K. R. An FK506-sensitive transporter selectively decreases intracellular levels and potency of steroid hormones. *J Biol Chem* **271**, 17152-17156 (1996). https://doi.org:10.1074/jbc.271.29.17152

30 Wagner, M., Smits, S. H. J. & Schmitt, L. In vitro NTPase activity of highly purified Pdr5, a major yeast ABC multidrug transporter. *Sci Rep* **9**, 7761 (2019). https://doi.org:10.1038/s41598-019-44327-8

31 Hovers, J. *et al.* A class of mild surfactants that keep integral membrane proteins water-soluble for functional studies and crystallization. *Mol Membr Biol* **28**, 171-181 (2011). https://doi.org:10.3109/09687688.2011.552440

32 Nguyen, K. A. *et al.* Glycosyl-Substituted Dicarboxylates as Detergents for the Extraction, Overstabilization, and Crystallization of Membrane Proteins. *Angew Chem Int Ed Engl* **57**, 2948-2952 (2018). https://doi.org:10.1002/anie.201713395

33 Pata, J. *et al.* Purification and characterization of Cdr1, the drug-efflux pump conferring azole resistance in *Candida* species. *Biochimie* **220**, 167-178 (2023). https://doi.org:10.1016/j.biochi.2023.12.007

34 Ernst, R. *et al.* A mutation of the H-loop selectively affects rhodamine transport by the yeast multidrug ABC transporter Pdr5. *Proc Natl Acad Sci U S A* **105**, 5069-5074 (2008). https://doi.org:10.1073/pnas.0800191105

35 Golin, J. *et al.* Studies with novel Pdr5p substrates demonstrate a strong size dependence for xenobiotic efflux. *J Biol Chem* **278**, 5963-5969 (2003). https://doi.org:10.1074/jbc.M210908200

36 Loo, T. W. & Clarke, D. M. Vanadate trapping of nucleotide at the ATP-binding sites of human multidrug resistance P-glycoprotein exposes different residues to the drug-binding site. *Proc Natl Acad Sci U S A* **99**, 3511-3516 (2002). https://doi.org:10.1073/pnas.022049799

37 Baghel, P. *et al.* Multidrug ABC transporter Cdr1 of *Candida albicans* harbors specific and overlapping binding sites for human steroid hormones transport. *Biochim Biophys Acta Biomembr* **1859**, 1778-1789 (2017). https://doi.org:10.1016/j.bbamem.2017.05.011

38 Krishnamurthy, S., Gupta, V., Snehlata, P. & Prasad, R. Characterisation of human steroid hormone transport mediated by Cdr1p, a multidrug transporter of Candida albicans, belonging to the ATP binding cassette super family. *FEMS Microbiol Lett* **158**, 69-74 (1998). https://doi.org:10.1111/j.1574-6968.1998.tb12802.x

39 Prescher, M. *et al.* Evidence for a credit-card-swipe mechanism in the human PC floppase ABCB4. *Structure* **29**, 1144-1155.e1145 (2021). https://doi.org:10.1016/j.str.2021.05.013

40 Afonine, P. V. *et al.* Conformational space exploration of cryo-EM structures by variability refinement. *Biochim Biophys Acta Biomembr* **1865**, 184133 (2023). https://doi.org:10.1016/j.bbamem.2023.184133

41 Egner, R., Rosenthal, F. E., Kralli, A., Sanglard, D. & Kuchler, K. Genetic separation of FK506 susceptibility and drug transport in the yeast Pdr5 ATP-binding cassette multidrug resistance transporter. *Mol Biol Cell* **9**, 523-543 (1998). https://doi.org:10.1091/mbc.9.2.523

42 Egner, R., Bauer, B. E. & Kuchler, K. The transmembrane domain 10 of the yeast Pdr5p ABC antifungal efflux pump determines both substrate specificity and inhibitor susceptibility. *Mol Microbiol* **35**, 1255-1263 (2000). https://doi.org:10.1046/j.1365-2958.2000.01798.x

43 Kueppers, P., Gupta, R. P., Stindt, J., Smits, S. H. & Schmitt, L. Functional impact of a single mutation within the transmembrane domain of the multidrug ABC transporter Pdr5. *Biochemistry* **52**, 2184-2195 (2013). https://doi.org:10.1021/bi3015778

44 Nim, S. *et al.* Atomic modelling and systematic mutagenesis identify residues in multiple drug binding sites that are essential for drug resistance in the major *Candida* transporter Cdr1. *Biochim Biophys Acta* **1858**, 2858-2870 (2016). https://doi.org:10.1016/j.bbamem.2016.08.011

45 Niimi, M., Niimi, K., Tanabe, K., Cannon, R. D. & Lamping, E. Inhibitor-Resistant Mutants Give Important Insights into Candida albicans ABC Transporter Cdr1 Substrate Specificity and Help Elucidate Efflux Pump Inhibition. *Antimicrob Agents Chemother* **66**, e0174821 (2022). https://doi.org:10.1128/AAC.01748-21

46 Takaine, M., Ueno, M., Kitamura, K., Imamura, H. & Yoshida, S. Reliable imaging of ATP in living budding and fission yeast. *J Cell Sci* **132** (2019). https://doi.org:10.1242/jcs.230649

47 Punjani, A. & Fleet, D. J. 3D variability analysis: Resolving continuous flexibility and discrete heterogeneity from single particle cryo-EM. *J Struct Biol* **213**, 107702 (2021). https://doi.org:10.1016/j.jsb.2021.107702

48 Alhumaidi, M. *et al.* Residues forming the gating regions of asymmetric multidrug transporter Pdr5 also play roles in conformational switching and protein folding. *J Biol Chem* **298**, 102689 (2022). https://doi.org:10.1016/j.jbc.2022.102689

Acknowledgments

We thank Pr. Dominique Sanglard for the gift of clinical isolates of *Candida glabrata* DSY562 and DSY565. We also gratefully acknowledge support from the CNRS/IN2P3 Computing Center (Lyon - France) for providing computing and data-processing resources needed for this work." A special thanks to Alexis Michon and his team for management of the IBCP computing facilities.

This work used the platforms of the Grenoble Instruct-ERIC center (ISBG; UAR 3518 CNRS-CEA-UGA-EMBL) within the Grenoble Partnership for Structural Biology (PSB), supported by FRISBI and GRAL, financed within the University Grenoble Alpes graduate school (Ecoles Universitaires de Recherche).

Funding

J.P.'s Ph. D was supported by the doctoral school EDISS 205 and R&D BOOSTER – IMABGEN grants,

Agence Nationale de la Recherche (Française), ((French) National Research Agency): ANR-24-CE44-3527 RESTOR to PFA and ABO as coordinators and VCH, RTE, EBE and SAG as partners,

Auvergne-Rhone-Alpes Region innovation program: R&D booster to PFA, VCH, MDU and AMO,

INSTRUCT-ERIC grant number 24618 to VCH, PFA, LZE and GSH,

FRISBI (ANR-10-INBS-0005-02) and GRAL, financed within the University Grenoble Alpes graduate school (Ecoles Universitaires de Recherche) CBH-EUR-GS (ANR-17-EURE-0003) to GSH and LZE.

The IBS-ISBG EM facility is supported by the Auvergne-Rhône-Alpes Region, the Fondation Recherche Medicale (FRM), the fonds FEDER and the GIS-Infrastructures en Biologie Santé et Agronomie (IBISA),

The Knut and Alice Wallenberg foundation (2023.0201) and the Swedish research council (2021-03992) to BWI and MHO.

Author contributions

Conceptualization: PFA, JPA, VCH

Methodology: PFA, JPA, VCH, BWI, EZA, RBA, NSA, CDE, AMO, ABA, SAG, EBE, MDU, RTE, ELA,

Investigation: PFA, JPA, VCH, BWI, EZA

Funding acquisition: PFA

Project administration: PFA

Supervision: PFA

Writing – original draft: PFA, JPA, VCH

Writing – review & editing: PFA, JPA, VCH, BWI, EZA, RBA, NSA, CDE, AMO, ABA, SAG, EBE, MDU, RTE, GSH, MHO, ABO, ELA, RCA, RPR

Competing interests: Authors declare that they have no competing interests.

Materials & Correspondence

Material and correspondence should be addressed to Pierre Falson and Vincent Chaptal.

Movies

Movie 1

Movie 1. Movie showing the conformation transition from frame 1 to frame 20 of *Cg*Cdr1 particles population in component 0 from the closed [^{s}0 |^{nc}ATP|^{c}ADP-Vi-Mg] to the open [^{s}0 |^{nc}ATP|^{c}ADP-Mg] states. The movie starts with the density maps and then the corresponding 3D-models, from the catalytic to the non-catalytic sides.

Movie 2

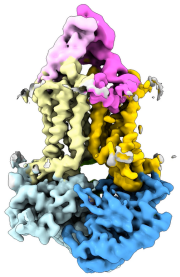

Movie 2. Movie showing the conformation transition from frame 1 to frame 20 of *Cg*Cdr1 particles population in component 1 from the closed [^{s}0 |^{nc}ATP|^{c}ADP-Vi-Mg] to the open [^{s}0 |^{nc}ATP|^{c}ADP-Mg] states. The movie starts with the density maps and then the corresponding 3D-models, from the catalytic to the non-catalytic sides.

Data and materials availability:

3D Data from variability refinements have been deposited in the public database Zenodo (see Supplementary Table 2). Other data are available in the main text or the supplementary materials.

Supplementary Materials

Materials and Methods

Supplementary Figures 1 to 16

Supplementary Tables 1 and 2

References (*53-58*)

Supplementary Movies 1 to 3

Extended Data 1 to 4